SUPPLEMENT TO THE *WELDING JOURNAL,* MONTH YEAR
Sponsored by the American Welding Society and the Welding Research Council

Evaluation of Correlations between DP-GMAW Process Parameters and Bead Geometry

Higher mean current, higher pulse frequency, lower thermal pulse frequency, and standard arc voltage may generate optimum bead geometry when using double pulsed gas metal arc welding

BY M. SEN, M. MUKHERJEE, AND T. K. PAL

ABSTRACT

In this study, an attempt has been made to evaluate the complex correlations occurred between double pulsed gas metal arc welding (DP-GMAW) process parameters and weld bead geometry using two statistical methods: Taguchi orthogonal array design method and response surface methodology. The Taguchi method was applied to plan the design of experiments (DoE). Contour and surface plots were made using response surface methodology (RSM) to understand the effect of different parameters on the bead geometry. It was found that at a particular range of arc voltage higher mean current, higher pulse frequency along with lower thermal pulse frequency produced optimum conditions for high depth of penetration with low or moderate bead width and height. The optimization of process parameters was also conducted using RSM and the optimum parameters were compared with experimental trials. Three second-order statistical models were also developed using experimental results to predict the weld bead parameters from the process parameters. The model developed was checked for its adequacy using ANOVA. Results of confirmation experiments showed that the model can predict the bead geometry with reasonable accuracy.

KEYWORDS

- DP-GMAW • Bead Geometry • Taguchi Method
- Response Surface Methodology

Introduction

The demand for quality products has led to the rapid advancement of today's manufacturing environments. The total quality index of a product depends on the quality of output from each subprocess involved in the production chain, and obviously, welding is one of the important subprocesses in most of the cases. The weld quality mainly depends on the weld bead geometry, mechanical properties, distortion of the welded joint, and deposition efficiency. All of these quality characteristic parameters are directly related to welding process parameters. Arc welding is a major joining process in modern manufacturing industries such as mining industry for bulk transport, road and rail transport, power generation, petrochemical, pulp and paper industries, and construction industries. Among the various types of arc welding, pulsed gas metal arc welding (GMAW-P) is being increasingly used for joining a wide variety of ferrous and nonferrous materials in industries due to its inherent advantages such as deep penetration, smooth weld bead, high welding speed, large metal deposition rate, lower spatter, lower distortion and shrinkage, and lesser probability of porosity and fusion defects (Refs. 1, 2). Smati (Ref. 3) also remarked that it is an advanced spray transfer process with low mean current. Thus, the GMAW-P is becoming increasingly popular for use in modern robotics and automated industries. In the pulsed GMAW process, welding current is pulsed between high and low levels of short or long time intervals so that it brings the weld zone to the melting point during the pulse current period and allows the molten weld pool to cool and solidify during the background current period. The primary parameters of a current pulse are peak current (I_p), background current (I_b), peak current duration (t_p), background current duration (t_b), and pulse frequency (f), as shown in Fig. 1 (Ref. 4). Other process parameters such as welding speed, pulse current, welding voltage, wire feed rate, electrode extension, and welding gun angle also influence the process behavior and the weld bead shape during welding in GMAW-P (Ref. 5). Pulsed current gas metal arc welding (GMAW-P) provides higher production efficiency and excellent controllability of droplet transfer. Pires et al. (Ref. 6) have mentioned that in GMAW-P the droplet is usually controlled by pulsed current and duration with "one drop per pulse" (ODPP), which makes it possible to improve the stability of welding process and the quality of the weld joint.

However, the range of the peak cur-

M. SEN is a postgraduate student, M. MUKHERJEE is a senior research fellow, and T. K. PAL (tkpal.ju@gmail.com) *is a professor, Metallurgical and Material Engineering Department, Jadavpur University, Kolkata, India.*

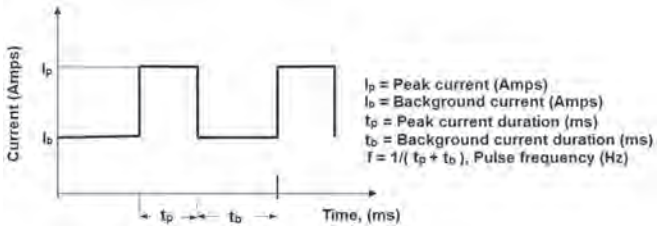

Fig. 1 — Pulsed GTAW process parameters (Ref. 4).

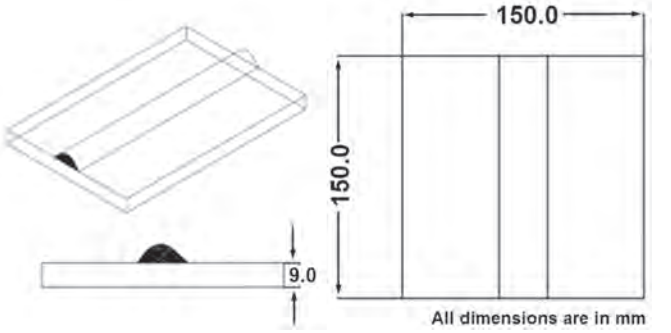

Fig. 3 — Dimension of base plates used for preparing bead on plates.

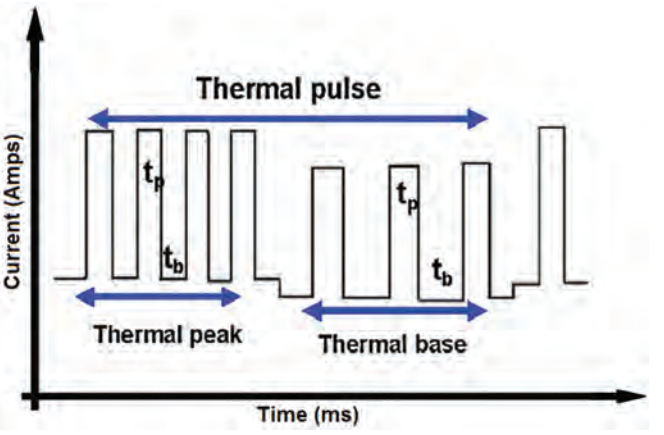

Fig. 2 — A schematic diagram of DP-GMAW electrical waveform (Ref. 11).

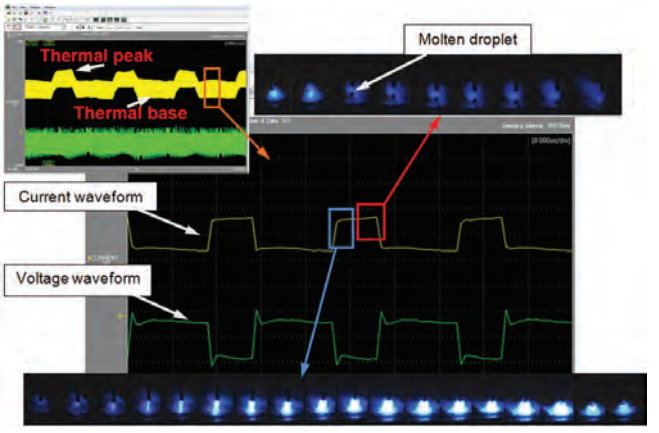

Fig. 4 — Typical oscilloscope and high-speed video camera record of weld run R2 reveals thermal peak and thermal base with ODPP mode of metal transfer.

rent duration for generating ODPP is narrow. If the duration of the peak-current period is longer, multiple drops may be detached in a single pulse, resulting in a streaming spray transfer. Or, if the duration is shorter, one droplet in multiple pulses (ODMP) may occur. To overcome the uncertainty of ODPP in conventional GMAW-P due to the narrowness of the optimal range, Zhang et al. (Ref. 7) have proposed a modified GMAW-P power source with an active metal transfer control. In this process, a pulse cycle is divided into two periods: growth period and detachment period. In the growth period, a current waveform, which is designed based on the desired average current and is below the transition current, is used. When the growth period ends, current is switched to the base level and the process enters the detachment period. The sudden change in welding current causes the droplet to oscillate vertically. When the droplet moves down, the current is switched back to the peak level. The increased electromagnetic force and downward momentum concludes the active droplet detachment in ODPP and eliminates the need for a very high current to detach the droplet, which is conventionally used in GMAW-P Xiao et. al. (Refs. 8–10). It further modified the original multi-pulse waveform of active metal transfer mechanism by incorporating a longer base period after the exciting pulse known as "active droplet oscillation method" and detaching phase delay period known as "enhanced active metal transfer" to maximize the oscillation and detachment efficiency of the molten droplets.

These advanced metal transfer mechanisms are using multiple active pulses within a pulse cycle to achieve easy control of the droplet characteristics in ODPP mode of metal transfer compared to conventional GMAW-P process. However, these techniques do not deal with the weld pool stirring mechanism, which actively controls the fluidity of the weld pool (Ref. 11).

Recently, Liu et al. (Refs. 11, 12) and Mendes da Silva et al. (Ref. 13) explored the double pulsed GMAW (DP-GMAW) process for aluminium alloys, where a low-frequency current pulsation or the thermal pulse is superimposed on a pulsed current for active metal transfer control and weld pool stirring. The main feature of the DP-GMAW is the simultaneous use of a high-frequency pulse (HFP) and thermal pulse (f_t). The schematic of DP-GMAW waveform is shown in Fig. 2 (Ref. 11).

The pulse frequency, peak, and base value of HFP are cyclically varied with thermal pulse fluctuation. The role of the HFP is to maintain the arc stability and the droplet transfer behavior especially to ensure one droplet transfer per pulse (ODPP) during welding operation. The thermal pulse (i.e., low-frequency pulse) is used to modulate duration of the high frequency pulses to improve the weld pool stirring, which guarantees forming of the weld bead ripple and expanding the range of weld joint root opening (Ref. 12). Mendes da Silva and Scotti (Ref. 13) have also mentioned that an effective fusion of the base metal and a good weld joint with regular ripple surface

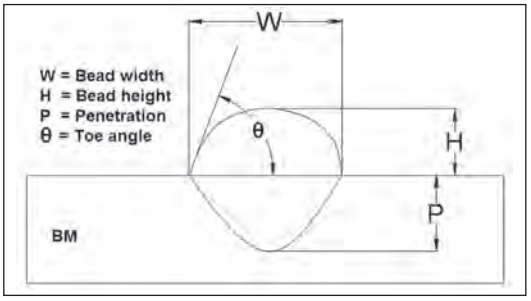

Fig. 5 — A schematic diagram of weld bead geometry.

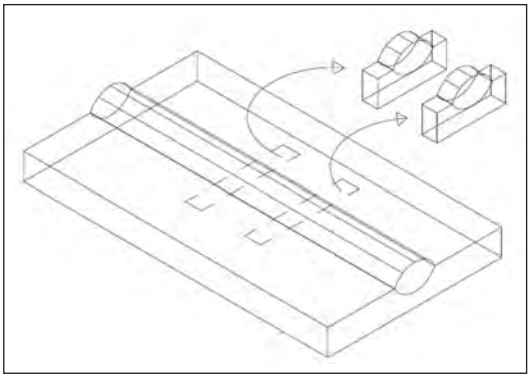

Fig. 6 — A schematic diagram of extracted specimens for bead geometry analysis.

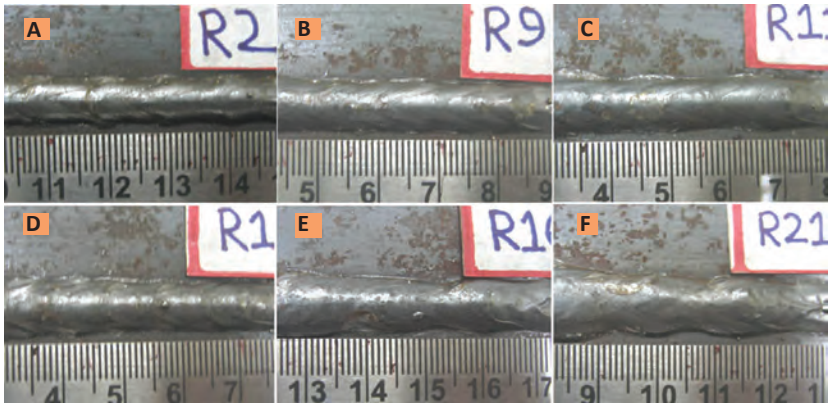

Fig. 7 — Typical images of weld bead appearances under different welding conditions. A — R2 (at f_t = 0.6 Hz, I_m = 220 A, f = 120 Hz, and V = 23); B — R9 (at f_t = 1.0 Hz, I_m = 240 A, f = 70 Hz, and V = 32); C — R11 (at f_t = 0.4 Hz, I_m = 260 A, f = 270 Hz and V = 26); D — R13 (at f_t = 0.8 Hz, I_m = 260 A, f = 120 Hz, and V = 32 V); E — R16 (at f_t = 0.4 Hz, I_m = 280 A, f = 120 Hz, and V = 29); and, F — R21 (at f_t = 0.4Hz I_m = 300 A, f = 220 Hz and V = 32 V).

can be obtained with the DP-GMAW process.

Pires et al. (Ref. 6) have compared the DP-GMAW process with GMAW-P and conventional GMAW process and listed some advantages as follows: 1) wider adjusting range, 2) capability to all-position welding, 3) wider root opening configuration, 4) reduce overall heat input, 5) improve joint properties, 6) strong weld pool stirring, and 7) reduce crack sensitivity.

Again, the welding process and parameters play a decisive role in controlling the bead geometry. Weld bead geometry is the first indication of the weld bead quality. The present trend in the fabrication industries is the use of automated welding processes to obtain high production rates and high precision. To automate a welding process it is essential to establish the relationship between process parameters and weld bead geometry to predict and control weld bead quality. Weld bead geometry includes the weld bead width (W), the weld bead height (H), and the depth of penetration (P). These elements, W, H, and P are sensitive to the welding processes and several input parameters. The relationship between welding parameters and weld bead geometry is becoming complex, since a number of factors are involved (Ref. 14). Several researchers have applied various optimization methods through developing mathematical models to specify the relationship between the input parameters and bead geometry. In the last two decades, a design of experiment (DoE) technique has been used to carry out such optimization. Evolutionary algorithms and computational networks have also grown rapidly and been adapted for many applications in different areas. Several techniques such as fractional factorial technique, multiple regression analysis, response surface methodology (RSM), Taguchi method, and artificial neural network (ANN) were applied through several decades to develop an understanding of the relationship between bead geometry and input variables for conventional processes like GMAW, gas tungsten arc welding (GTAW), submerged arc welding (SAW), and advanced processes like GMAW-P, GTAW-P, and electron beam welding (EBW). Some researchers have also used combined techniques such as GA coupled with RSM, and multiple regression analysis coupled with ANN to effectively predict optimum condition for a particular process. Prior to 2008, Benyounis and Olabi (Ref. 15) explicitly reviewed some of these advanced methods and their application. Recently, Zhang et al. (Ref. 16) and Liu et al. (Refs. 17, 18) have developed a new advanced computer-based neuro-fuzzy model to simulate 3D weld pool surface and bead geometry correlated with the input variables in the conventional GTAW process. Through least squares algorithm-based statistical analyses, it was found that the optimal model was able to predict the width, length, and convexity of the 3D weld pool surface with acceptable accuracy.

However, the literature revealed that not much relevant work has been done in the area of bead geometry characteristics with DP-GMAW process parameters. The correlation between the bead geometry and the input variables of a DP-GMAW process is nonlinear, highly complex, interde-

Table 1 — Chemical Compositions (in wt-%) of Base Metal and Filler Metal

Type	C	Mn	Si	S	P	Cr	Ni	Mo	V	W	Cu	Al	B
Base Metal	0.147	0.79	0.02	0.011	0.014	0.036	0.019	0.001	0.0013	0.038	0.0078	0.057	0.0008
Filler Metal	0.099	1.13	0.64	0.011	0.01	0.052	0.84	0.006	0.001	0.049	0.405	0.003	0.0008

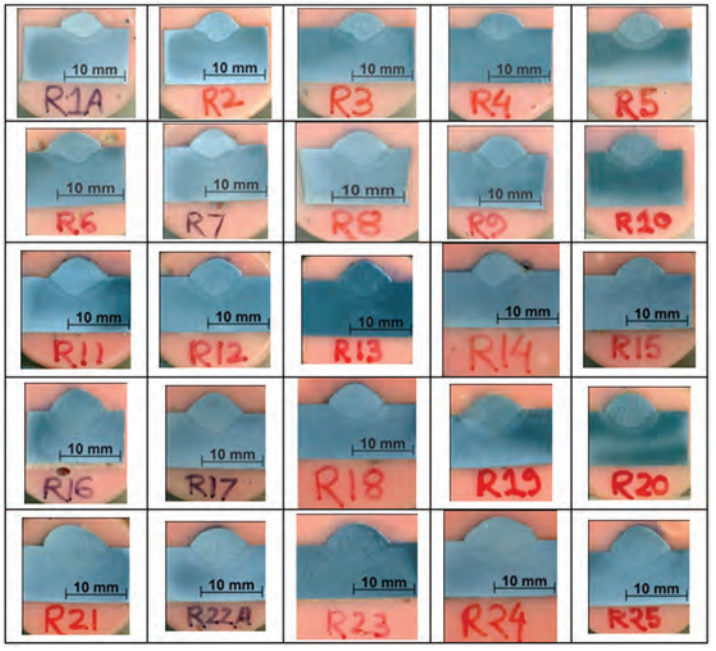

Fig. 8 — Images of sections of weld bead geometry under different welding conditions.

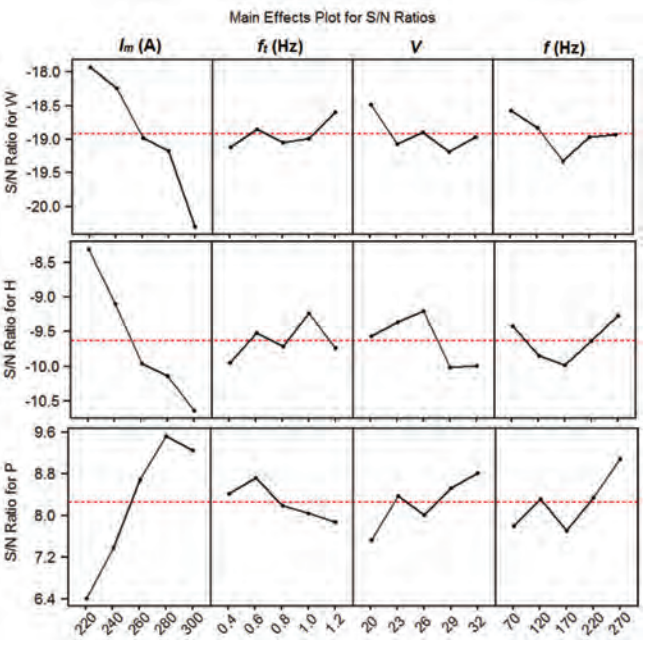

Fig. 9 — Effect of primary process parameters on bead geometry.

pendent and requires a large number of parameters to form DoE. Hence, the selection of an optimal welding parameter setting is critical and also very important from the point of view that it should ensure desired weld quality and reliability while enhancing productivity. Consequently, extensive research work is needed to develop a better scientific knowledge of the interdependent nature of DP-GMAW process parameters and its output to the weld quality, thus, the design engineers, manufacturers, fabricators, and scientists associated with this field can be benefited.

In this study, an attempt has been made to evaluate DP-GMAW process parameters for predicting and optimizing the weld bead geometry using two statistical methods: Taguchi orthogonal array design method, and response surface methodology. The main objective of this study is to get insight into the complex correlations occurring between DP-GMAW process parameters and weld bead geometry. Taguchi orthogonal array design has been employed for the development of design of experiments (DoE). The response surface methodology has been further used to develop the mathematical model to study the main and interaction effects of process parameters on bead geometry. Furthermore, optimization of process parameters was carried out using RSM to obtain optimum weld bead geometry using the developed models.

Design of Experiments

The general procedures that could be used to determine the optimal welding parameter settings are design of experiment (DoE) techniques such as fractional factorial design, D-optimal design, response surface methodology, and Taguchi method (Refs. 19, 20). Taguchi method has been successfully applied in the manufacturing field for nearly three decades to robustly design products or processes having a single quality parameter. Taguchi technique is based on orthogonal array (OA) of experiments and widely used in different fields of engineering to optimize the process parameters (Ref. 20). The integration of DoE with parametric optimization of process can be achieved in the Taguchi method. An OA provides a set of well-balanced experiments, and Taguchi's signal-to-noise (S/N) ratios, which are logarithmic functions of the desired output, serve as objective functions for optimization. Orthogonal array and S/N ratios are used to study the effects of control factors and noise factors and to determine the best quality characteristics for particular applications (Ref. 20). Among the several factors, mean current, pulse frequency, thermal pulse frequency, and arc voltage are considered in this study as the major influencing factors of a DP-GMAW process due to the fact that these parameters are the function of one and/or several individual parameters such as peak current, background current, peak current duration, and background current duration.

In this work, sufficient numbers of trial experiments have been carried out to find the parameter ranges in which effective welding took place without failure (such as power failure due to short circuit and discontinuous arcing). In order to evaluate the

Table 2 — Process Parameters and the Different Levels Used in Taguchi OA

Factors	Parameter	Unit	Level 1	Level 2	Level 3	Level 4	Level 5
1	I_m	A	220	240	260	280	300
2	f_t	Hz	0.4	0.6	0.8	1.0	1.2
3	V	V	20	23	26	29	32
4	f	Hz	70	120	170	220	270

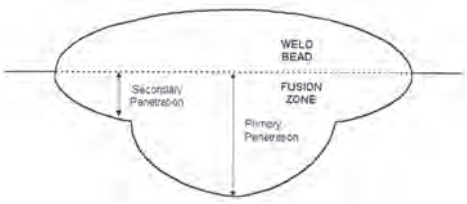

Fig. 10 — Schematic diagram of weld bead and fusion profile.

process parameters settings, the Taguchi method uses a statistical measure of performance, called signal-to-noise (S/N) ratio (η, dB). The standard S/N ratios generally used are categorized as nominal-is-best (NB), lower-the-better (LB), and higher-the-better (HB) criterion. Depending on the experimental objective, three weld bead geometries, i.e., the penetration, the width, and the height, are considered as major weld quality characteristics. In the case of bead width and height, lower values are desirable and follow the LB criterion. On the other hand, penetration follows the HB criterion. These S/N ratios in the Taguchi method are defined as follows.

$$\eta = -10 \log \left[\frac{1}{n} \sum_{i=1}^{n} y_i^2 \right]$$

(lower-the-better criterion) (1)

$$\eta = -10 \log \left[\frac{1}{n} \sum_{i=1}^{n} \frac{1}{y_i^2} \right]$$

(higher-the-better criterion) (2)

Where, y_i is the observed data at the ith trial and n is the number of trials.

In recent years, Taguchi's approach has become one of the most powerful methods of statistical design of experiment (DoE) techniques. Several researchers have also used Taguchi's OA experiment for selection of optimum levels of process parameter setting in different welding processes to get desired bead geometry and weld quality (Refs. 21–23). However, Montgomery (Ref. 24) has noted that the experimental design methods frequently become too complex and a large number of experiments have to be carried out as the number of process parameters increases.

Nevertheless, the experimental optimization of any welding process is often a very costly and time consuming task, due to many kinds of nonlinear events involved. To solve this problem, the response surface methodology (RSM) is often used, in which the experimenter tries to approximate the unknown mechanism with an appropriate empirical model (Refs. 25, 26). Response surface methodology is an empirical modeling approach using polynomials as local approximations to the true input/output relationship. This empirical approach is often adequate for process improvement in an industrial setting. By careful design of experiments, the objective is to optimize a response (output variable) that is influenced by several input variables (input parameters). An experiment is a series of tests, called runs, in which changes are made in the input variables in order to identify the reasons for changes in the output response.

The relationship between the response variable of interest (y), and the input variables ($x_1, x_2, \ldots, x_n$) is usually not known. In general, if all the variables are assumed to be measurable, the experimenter approximates the system function with an empirical model of the form

$$y = f(x_1, x_2, x_3, \ldots\ldots, x_{n-1}, \ldots., x_n) \quad (3)$$

where f is a first- or second-order polynomial. This empirical model is known as response surface model. The variables are known as natural variables since they are expressed in physical units of measurement. In the RSM, the natural variables are transformed into coded variables that are dimensionless. The successful application of RSM relies on the identification of a suitable approximation for f.

In the practical application of RSM, it is necessary to develop an approximating model for the true response surface. The approximating model is based on observed data from the process or system and is an empirical model. Multiple regression is a collection of statistical techniques useful for building the types of empirical models required in RSM. Usually, a second-order polynomial Equation 4 is used in RSM

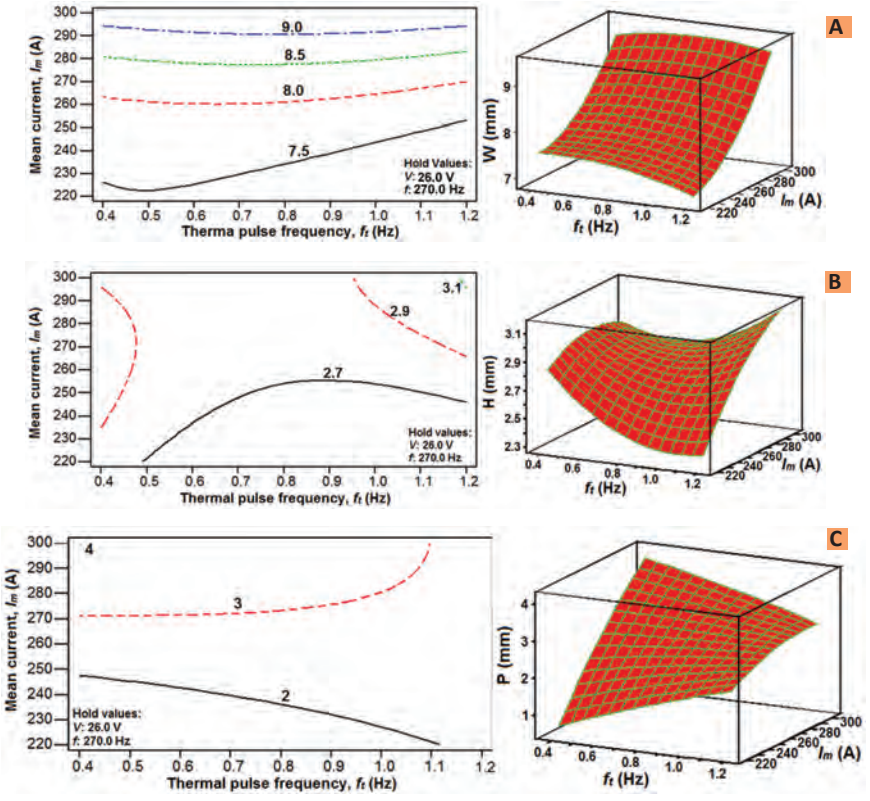

Fig. 11 — Contour and surface plot shows the effect of I_m and f_t on the following: A — bead width; B — bead height; C — depth of penetration; at constant values of f = 270 Hz, and V = 26.

Table 3 — The Design Matrix for Experimental Run and Other DP-GMAW Process Parameters

Sl no.	I_m (A)	f_t (Hz)	V	f (Hz)	v_w (m/min)	I_p(A)	I_b(A)	t_p (ms)	t_b (ms)	HI (kJ/mm)
R1	220	0.4	20	70	5	275.2	180	6.0	8.3	0.528
R2	220	0.6	23	120	5	346.7	180	2.0	6.3	0.607
R3	220	0.8	26	170	5	336.9	180	1.5	4.4	0.686
R4	220	1	29	220	5	361.8	180	1.0	3.5	0.766
R5	220	1.2	32	270	5	328.1	180	1.0	2.7	0.845
R6	240	0.4	23	170	5.8	356.9	200	1.5	4.4	0.662
R7	240	0.6	26	220	5.8	381.8	200	1.0	3.5	0.749
R8	240	0.8	29	270	5.8	348.1	200	1.0	2.7	0.835
R9	240	1	32	70	5.8	295.2	200	6.0	8.3	0.922
R10	240	1.2	20	120	5.8	366.7	200	2.0	6.3	0.576
R11	260	0.4	26	270	6.6	368.1	220	1.0	2.7	0.811
R12	260	0.6	29	70	6.6	315.2	220	6.0	8.3	0.905
R13	260	0.8	32	120	6.6	386.7	220	2.0	6.3	0.998
R14	260	1	20	170	6.6	376.9	220	1.5	4.4	0.624
R15	260	1.2	23	220	6.6	401.8	220	1.0	3.5	0.718
R16	280	0.4	29	120	7.4	406.7	240	2.0	6.3	0.974
R17	280	0.6	32	170	7.4	396.9	240	1.5	4.4	1.075
R18	280	0.8	20	220	7.4	421.8	240	1.0	3.5	0.672
R19	280	1	23	270	7.4	388.1	240	1.0	2.7	0.773
R20	280	1.2	26	70	7.4	335.2	240	6.0	8.3	0.874
R21	300	0.4	32	220	8.2	441.8	260	1.0	3.5	1.152
R22	300	0.6	20	270	8.2	408.1	260	1.0	2.7	0.720
R23	300	0.8	23	70	8.2	355.2	260	6.0	8.3	0.828
R24	300	1	26	120	8.2	426.7	260	2.0	6.3	0.936
R25	300	1.2	29	170	8.2	416.9	260	1.5	4.4	1.044

Note: I_m = mean current, f_t = thermal pulse frequency, V = voltage, f = pulse frequency, v_w = wire feed speed, I_p = peak current, I_b = background current, t_p = peak time, $_b$ = background time, HI = he t input (I_m × V × η × 60/welding speed × 1000).

$$y = \beta_0 + \sum_{i=1}^{n} \beta_i x_i + \sum_{i=1}^{n} \beta_{ii} x_i^2 + \sum_{i} \sum_{j} \beta_{ij} x_i x_j + \varepsilon \quad (4)$$

where ε is a random error, and β_{ij} = 0, 1, 2....*n* are the regression coefficients.

The application of RSM in many areas of welding processes to predict and to optimize bead geometry as a function of process parameters was the interest of many researchers (Refs. 27–30). However, there are practically no studies reported on the bead geometry of DP-GMAW process using sequential design of experiments employing the Taguchi and RSM, and no numerical models correlating DP-GMAW process parameters with bead parameters like depth of penetration, bead width, and bead height were developed.

Experimental Procedure

Sample Preparation to Make Weld Beads

In the present work, a mild steel plate having 0.15% carbon of size 150 × 150 × 9 mm was used as base metal to prepare bead on plates using ER80S-G, a commercially available uncoated welding wire of diameter 1.2 mm. Details of bead-on-plate preparation for the DP-GMA welding process are shown in Fig. 3. The chemical composition of the base metal and welding wire are given in Table 1.

Process Parameter Variation in DP-GMAW

The control factors or process parameters and their different levels are shown in Table 2. The design matrix was made using Taguchi's L25 (5 levels*4 factors) OA design as given in Table 3 along with other operating parameters. The typical DP-GMAW process with selected welding parameters was secured using the oscilloscope and high-speed video camera as shown in Fig. 4. Figure 4 reveals that the thermal peak and thermal base appeared during the process along with one drop per pulse (ODPP) transfer in single pulsation. In this study, four important DP-GMAW process parameters such as mean current (I_m), thermal pulse frequency (f_t), arc voltage (V) and pulse frequency (f) were selected and varied as per DoE. Mean current (I_m), thermal pulse frequency (f_t), and pulse frequency (f) can be defined by the following equations:

$$I_m = \frac{I_p t_p + I_b t_b}{t_p + t_b} \quad (5)$$

$$f = \frac{1}{t_p + t_b} \quad (6)$$

$$f_t = \frac{1}{\text{Thermal peak time} + \text{Thermal base time}} \quad (7)$$

However, the equation neglects any variation in set values (selected process parameters) due to the instantaneous changes in the double pulse functions that may occur during operation. Either t_p or t_b can be preset due to the machine constraints, i.e.; constant or factory curve feature, and these two parameters are varied with

the pulse frequency. Again, in the welding machine, thermal peak time and thermal base time can only be expressed as a function of thermal pulse frequency.

Welding Procedure

The experiments were conducted using a Kemppi, (Finland make) water-cooled Universal MIG/MAG machine (Model: KEMPPI FASTMIG Pulse 450) using DC electrode positive (DCEP). The welding conditions and process parameters used (as per DoE) are given in Table 3. Bead-on-plate welding was performed using the selected welding parameters in a double pulsed GMAW process. To ascertain the operating mode, oscilloscope (Model: DLM2000; Make: Yokogawa Electronic Co., Japan) and high-speed video camera (Model: Phantom V311, Make: Vision Research Inc., USA) were used to record current pulsation, voltage, frequency, and drop transfer respectively during each welding run. The welding operations were performed using 92% Ar + 8% CO_2 shielding gas mixture. A contact tip to workpiece distance (CTWD) was maintained at 18 mm for all the weld deposits. A welding speed of 400 mm/min was also maintained during the operation. All necessary care was taken to avoid distortion and the welding was made with applying proper clamping (i.e., pneumatic grip and C-clamp) devices.

Metallographic Sample Preparation and Bead Geometry Measurement

Once the welding was over, all welded plates were cut perpendicular to the welding direction using a power saw machine to measure the weld bead geometry. A schematic diagram of the bead geometry is shown in Fig. 5. Two specimens (cross-sectional specimen centering the weld axis) were cut from each plate 5 cm away from the start and the end point as shown in Fig. 6. The cut surfaces were flattened through belt grinding and were polished successively with 120-, 180-, 220-, 320-, 400-, 600-, 800-, 1000-, and 1200-grit silicon carbide abrasive papers. The specimens were further polished in a polishing wheel

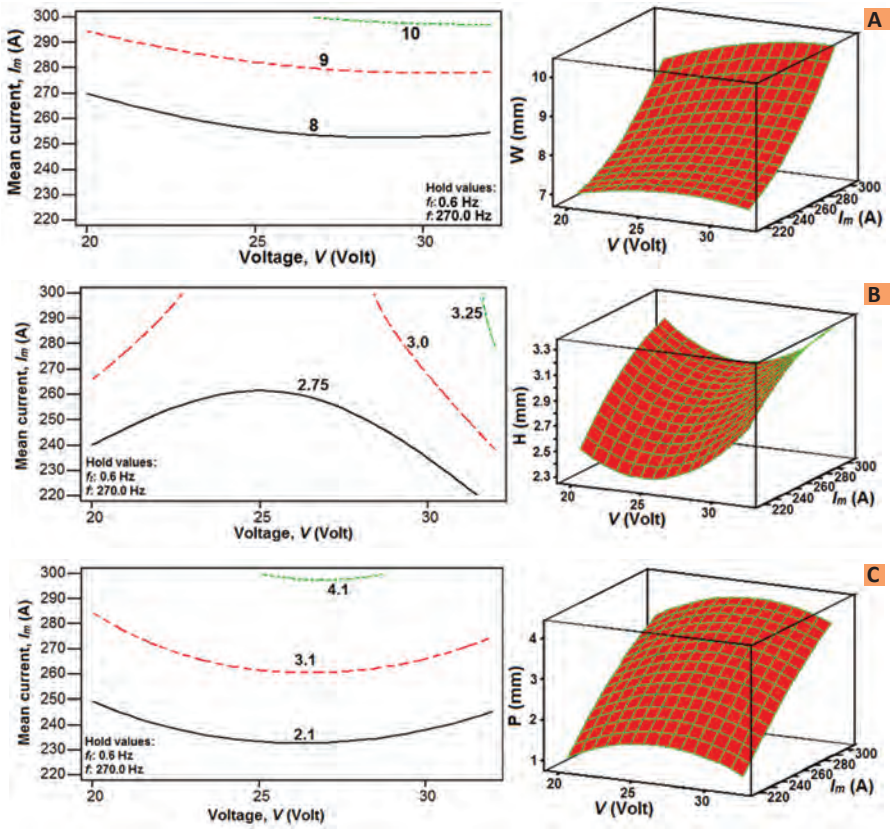

Fig. 12 — Contour and surface plot shows the effect of I_m and V on the following: A — bead width; B — bead height; C — depth of penetration; at constant values of i = 0.6 Hz and f = 270 Hz.

Table 4 — Complete Weld Bead Geometry Parameters of Each Welding Conditio

Sl no.	W (mm)	H (mm)	P (mm)	Toe angle (θ)	P/W rati	H/W rati
R1	7.17	2.59	1.561	49.5	0.218	0.361
R2	8.17	2.68	2.312	44	0.283	0.329
R3	8.35	2.43	2.348	46.5	0.281	0.292
R4	8.15	2.52	2.164	50.5	0.265	0.310
R5	7.59	2.81	2.194	51	0.289	0.370
R6	8.66	2.93	2.247	35.5	0.259	0.339
R7	8.11	2.85	2.000	53.5	0.246	0.352
R8	8.26	2.85	2.623	52.5	0.318	0.346
R9	8.13	2.82	2.546	58.5	0.313	0.347
R10	7.66	2.80	2.339	60	0.305	0.366
R11	9.64	3.11	2.981	45	0.309	0.323
R12	8.88	3.06	3.098	60.5	0.349	0.345
R13	8.77	3.33	2.542	52.5	0.290	0.380
R14	8.84	3.30	2.239	49.5	0.253	0.374
R15	8.34	2.96	2.843	55	0.341	0.355
R16	9.26	3.67	3.322	60.5	0.359	0.396
R17	9.38	3.38	3.081	53	0.328	0.360
R18	9.18	3.39	2.707	59.5	0.295	0.369
R19	9.55	2.76	3.173	46	0.332	0.289
R20	8.14	2.95	2.741	63	0.336	0.362
R21	10.85	3.54	3.671	55.5	0.338	0.327
R22	9.36	3.03	3.461	54.5	0.370	0.324
R23	10.41	3.42	2.647	53.5	0.254	0.329
R24	9.99	3.15	2.634	44	0.263	0.315
R25	11.29	3.95	2.336	51.5	0.206	0.321

Note: W = bead width; H = top reinforcement height; P = penetration depth; /W = aspect ratio; H/W = onvexity index.

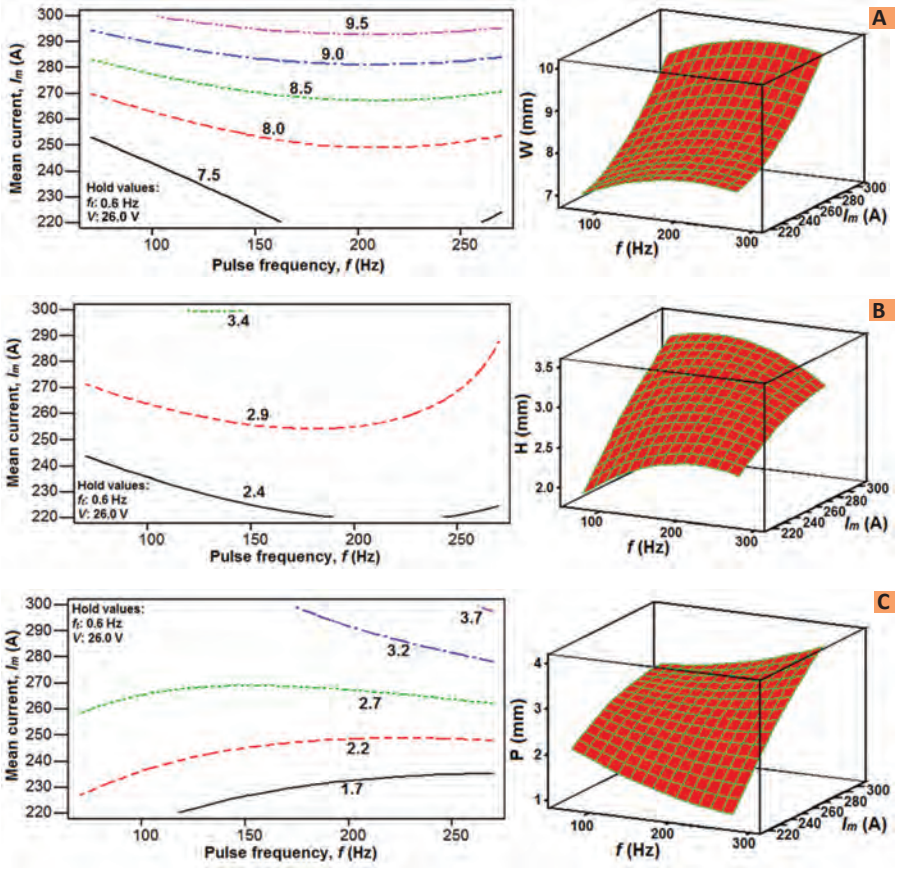

Fig. 13 — Contour and surface plot shows the effect of I_m and f on the following: A — Bead width; B — bead height; C — depth of penetration; at constant values of f_i = 0.6 Hz, and V = 26 Volt.

Table 5 — ANOVA Table for Response Surface Function of Bead Widt

Source	Degree of Freedom	Sum of Squares	Mean Square	F-Rati	P-Value
Model	20	21.1558	1.762980	5.75	0.002
Error	4	3.6825	0.306872		
Total	24	24.8382			

using diamond compound of 9-, 6-, 3-, 1-, and 0.25-micron wet Selvyt cloth/microcloth followed by final polishing with 0.05-micron slurry of Al_2O_3 (diluted by distilled water in 9:1 ratio) on a fine micro cloth. The specimens were then washed, cleaned with distilled water and ethanol, and dried by a drier. After polishing, those samples were etched with Nital solution (2% HNO_3). The bead geometry parameters were measured in a Carl Zeiss Microscope (5× magnification). The average values of weld bead width, height, and penetration (from the two cuts) were calculated for each experiment and the values are given in Table 4.

Results and Discussion

The macro views of the beads (bead appearance and bead geometry), welded with different process parameters (I_m, V, f, and f_t), were captured and shown in Figs. 7 and 8. The values of bead geometry such as bead height (H), bead width (W), and depth of penetration (P) were measured from the macrographs using *AutoCAD 2006* software and all the data are presented in Table 4. The aspect ratio or the maximum penetration depth to bead width ratio (P/W ratio) and convexity index or the reinforcement height to bead width ratio along with toe angles are also provided in Table 4. Concerning the index P/W, which indicates the bead slenderness, one could expect that the less slender the bead (higher ratio P/W), the less difficult for the gas to escape (Ref. 13). The P/W values in Table 4 suggest that the DP-GMAW technique should present less difficulty for pore trapping. Convexity index of the beads is computed using W and H (Table 4). The optimum level for a factor is the level that gives the desired quality characteristics in the experimental region. In this study, the desired quality characteristic for penetration is the bigger-the-better, and for convexity index, the desired quality characteristic is the-smaller-the-better.

Weld Bead Appearance

The bead appearance or the bead profile summarized in Fig. 7 shows that the ripples are formed on the joint surface. It can be anticipated that the typical rise and fall features of the ripples are similar to the electrical waveforms of the welding process. Thermal pulse was used to produce oscillation in weld pool to improve fluidity, leading to the ripple formation during the molten metal solidification. The ripple profile on the weld joint surface was related directly with the thermal pulse frequency. The thermal pulse (i.e., low frequency pulse) is used to modulate peak and duration of the high-frequency pulse and to improve the fluidity of the weld pool (Refs. 12, 13). Arc plasma force and heat input are varied with thermal pulse frequency, which guarantees forming of the weld bead ripple and expanding the range of weld joint clearance. A good bead on plate with regular ripple surface has been obtained with the DP-GMAW process. Therefore, with the increase of low-frequency pulses, the ripples on the joint surface became more prominent — Fig. 7. Furthermore, when observing the cross section of the weld beads as shown in Fig. 8, there was scattered variation of bead geometries, i.e., bead height, width, and depth of penetration along the longitudinal direction, indicating that other parameters along with thermal pulse have significant effect in controlling the geometry.

Taguchi Analysis

The Taguchi method was applied to understand the individual effect of process parameters on the weld bead geometry. In the present study, two criteria are typically followed: for bead width and bead height, the lower-the-better (LB) criterion and for the depth of penetration, the higher-the-better (HB) criterion. Consequently owing to the LB characteristics, the highest S/N ratio in each factor is desirable to obtain the minimum bead width and bead height, and because of the HB characteristics, the highest S/N ratio in each factor is required to attain the maximum depth of penetration. In general, higher is the difference between the minimum and the maximum S/N ratios in each factor, the higher is the effect on the bead geometry.

Figure 9 presents the calculated S/N ratios of four factors on the weld bead geometry according to each level. As shown in Fig. 9, the mean current (I_m) is a dominant parameter for all the bead geometry. However, the mean current has two-fold effect on the bead geometry. When considering minimum bead width and bead height as the prime response then the lowest I_m as a value of 220 A is desirable, but to get the maximum depth of penetration, higher I_m as a value of 280 A is required. This can be explained in terms of the lower melting rate of filler metal at low I_m, which leads to slower rate of molten filler metal droplets transferring into weld pool and consequently the bead geometry minimizes. On the other hand, high I_m increases the melting rate due to a higher heat input (Table 3) leading to a higher rate of molten filler metal droplets transferring into the molten weld pool, and thus the weld pool becomes superheated (Ref. 31). This superheated molten filler metal at single pulse condition increases the pinch effect of the droplet and enhances the depth of penetration. Apart from mean current, the thermal pulse frequency (f_t), the arc voltage (V), and pulse frequency (f) have secondary effect on the bead geometry. It is observed that the high f_t values ranging between 1.0–1.2 Hz result in minimum bead width and height, but maximum depth of penetration is attained at f_t value of 0.6 Hz. Conversely, to get the minimum W and H lower values of V and f are desirable; however, to get maximum P higher of these values is probably essential. It is also observed from Fig. 9 that the optimization of the process parameters (where the minimum W and H along with maximum depth of penetration can be achieved) is not possible due to variation in LB and HB characteristics of the bead geometry, and the Taguchi method simply ignores the parametric interactions. Therefore, RSM optimization tool considering 25 experiments were further used to get an accurate optimization process. Additionally, the viable process parameters obtained from the Taguchi method are further considered as constant input variables (for particular responses) to construct the response surfaces and contour plots in the RSM analysis to understand the effect of process parameters on the bead geometry.

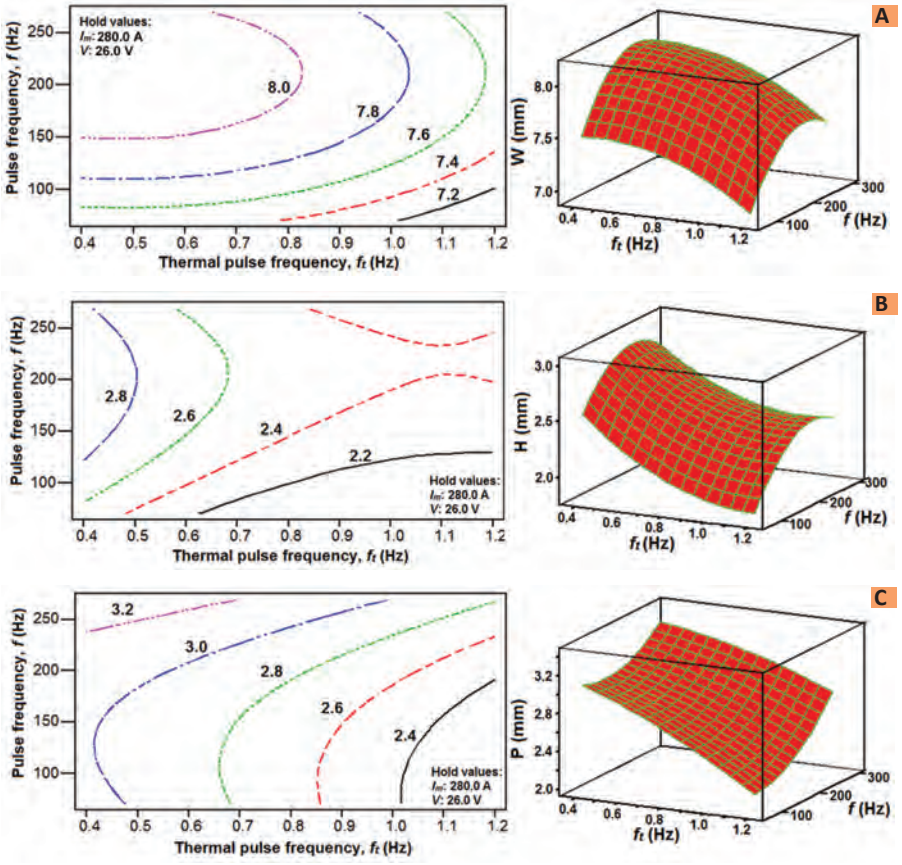

Fig. 14 — Contour and surface plot shows the effect of f and f_t on the following: A —bead width; B — bead height; C — depth of penetration; at constant values of I_m = 280 A and V= 26.

Table 6 — ANOVA Table for Response Surface Function of Bead Heig t

Source	Degree of Freedom	Sum of Squares	Mean Square	F-Rati	P-Value
Model	20	2.86383	0.238652	6.09	0.002
Error	4	0.47043	0.039203		
Total	24	3.33426			

The Evolution of Bead Geometry Using RSM

In this study, four process parameters (I_m, V, f, and f_t) were considered (Table 3) as the basic DP-GMAW process parameters (individual and cumulative parameters) that can significantly affect the heat transfer and fluid flow in the weld pool. Generally the weld fusion area or the weld pool area may be separated into two main regions. "Primary Penetration" is characterized by substantial penetration at the center of the fusion zone.

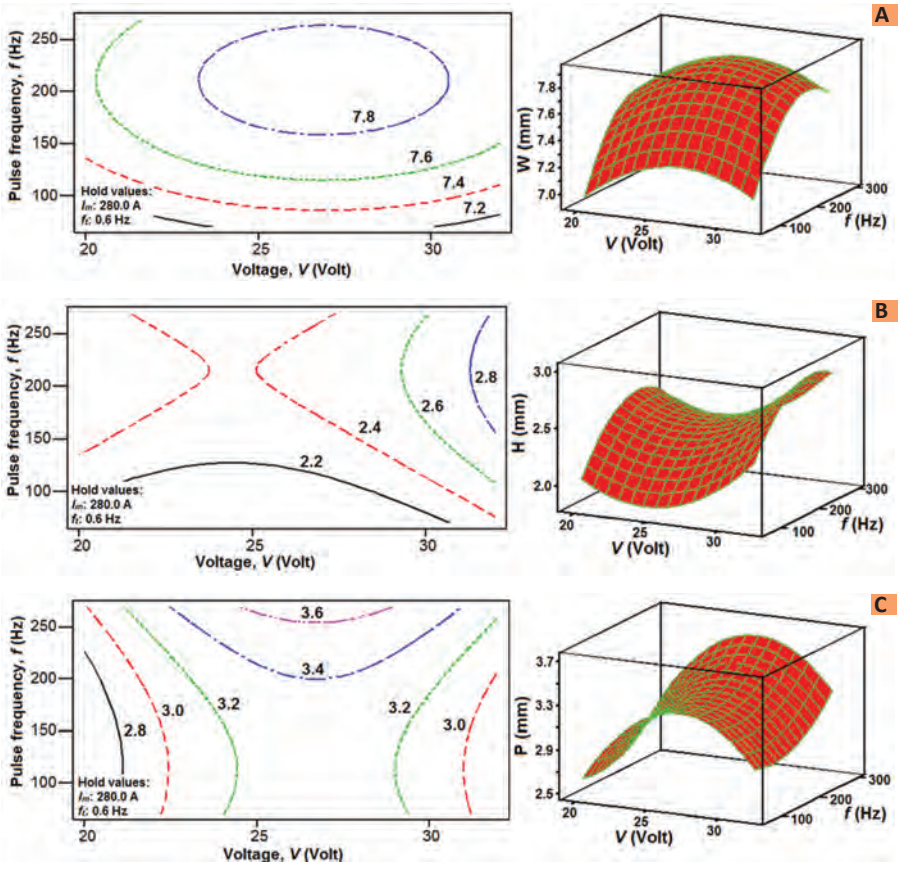

Fig. 15 — Contour and surface plot shows the effect of f and V on the follwing; A —bead width; B — bead height; C — depth of penetration, at constant values of I_m = 280 A and f_t = 0.6 Hz.

Table 7 — ANOVA Table for Response Surface Function of enetratio

Source	Degree of Freedom	Sum of Squares	Mean Square	F-Rati	P-Value
Model	20	5.36549	0.447124	13.25	0.001
Error	4	0.40497	0.033747		
Total	24	5.77046			

"Secondary Penetration" is caused by comparatively slow melting at the edges of the weld pool (Ref. 32). The typical profile of the penetration regions in a bead-on-plate weld is shown in Fig. 10. If the process parameters increase primary penetration then the depth of penetration should also be increased. Whereas, the increased secondary penetration simply boost the convexity index by sacrificing the depth of penetration. Essers and Walter (Ref. 33) stated that the heat is transferred to the workpiece from the arc column through convection, radiation, and conduction, along with the heat developed within the transferred droplet. In pulse spray transfer mode, the primary mode of metal transfer used in this study, liquid droplets transferred from the filler metal are superheated. Thus, the droplet transfer frequency coupled with the droplet heat content would contribute to the depth of primary penetration. Therefore, a suitable combination of primary and secondary penetration or profile is required to achieve acceptable bead geometry. By varying several process parameters and due to their combined effect, different bead profiles can be achieved.

Figure 11 shows the estimated response surfaces and contour plots for bead width (W), bead height (H), and depth of penetration (P) with varying values of I_m and f_t keeping f and V constant. Figure 11 clearly reveals that bead width, bead height, and depth of penetration increases with an increase in I_m at fixed f_t. However, at a particular higher I_m bead width is less sensitive to change in f_t, whereas bead height increases with increase in f_t and large depth of penetration can be achieved at lower f_t values. However, this variation was found to be reversed with a decrease in mean current at a constant thermal pulse frequency, especially for H and P. Furthermore, Figure 12A depicts that at a higher mean current level, the increase in arc voltage increases bead width of the weld deposit up to a certain level. Bead height initially decreases with increased arc voltage at particular mean current level and then increases — Fig. 12B. Also, from Fig. 12C, it is observed that at a particular mean current, the depth of penetration increases with an increase up to 25–28 V, and then decreases with the further increase in arc voltage. Again, Fig. 13 clearly represents that the pulse frequency has two-fold effects on bead geometry. Lower pulse frequency (ranging from 70 to 170 Hz) at higher mean current (above 250 A) significantly increases W and H, but the effect of pulse frequency on W and H become opposite as the frequency increases further — Fig. 13A and B.

On the other hand, Fig. 13C shows that the depth of penetration at lower pulse frequency can be high if the mean current is low, but at higher I_m increase in f significantly increases the depth of penetration. Figure 14 clearly depicts that increase in f_t values at particular pulse frequency decreases the overall bead geometry. Whereas high pulse frequency at low f_t significantly enhances the bead geometry. Maximum depth of penetration along with the lower bead width and height can be obtained within a particular range of these parameters (i.e., f = 200–260 Hz, f_t = 0.4–0.8 Hz). Figures 15 and 16 show that at a particular range of arc voltage (25–28 V) higher pulse frequency, along with lower thermal pulse frequency, are able to produce optimum conditions for high depth of penetration with low or moderate bead width and height.

The variation in bead geometry due

to the variation in process parameters can be explained by the variation in weld pool dimension and shape. Zacharia et al. (Ref. 34) have stated that the weld pool dimension and shape is critically controlled by individual and combined effect of several factors like fluid flow mechanism, drop temperature, arc temperature, drop transfer rate, droplet size, and drop acceleration. It is well established that these factors are the result of the variation in different process parameters. The fluid flow mechanism, which is a product of different driving forces, plays a deterministic role on controlling the weld pool that and shape. The effects of the different driving forces on the flow fields and weld pool dimensions that have been identified to date are illustrated schematically in Fig. 17. The magnitude and direction of the flow of molten metal in the weld pool can significantly alter the local heat transfer conditions, and consequently, the fusion zone geometry. The driving forces for fluid flow in the weld pool fall into two broad categories: the volume forcing terms that include the buoyant (thermal/gravity) forces and electromagnetic forces, and the shear and pressure acting on the weld pool surface due to surface tension gradient and surface curvature (Ref. 34). The fluid flow in the weld pool is also influenced by the arc pressure due to plasma. However, the arc pressure becomes important only when welding current is more than 350 A because at current over 350 A, the surface of the weld pool becomes markedly depressed and the assumption of negligible or flat surface is no longer valid (Ref. 35). Therefore, the arc pressure has not been considered in the present analysis, since the mean current used in the present study are below 350 A.

Again, the shear force due to the impinging of shielding gas flow, which remains constant during welding, is also considered to be negligible on the weld pool convection. Hence, in effect three major driving forces such as buoyancy force due to temperature-induced changes in density of the liquid, electromagnetic (Lorentz) forces due to the interaction of the arc current with its magnetic field (which forces fluid in a downwards motion), and Marangoni forces due to changes in surface tension

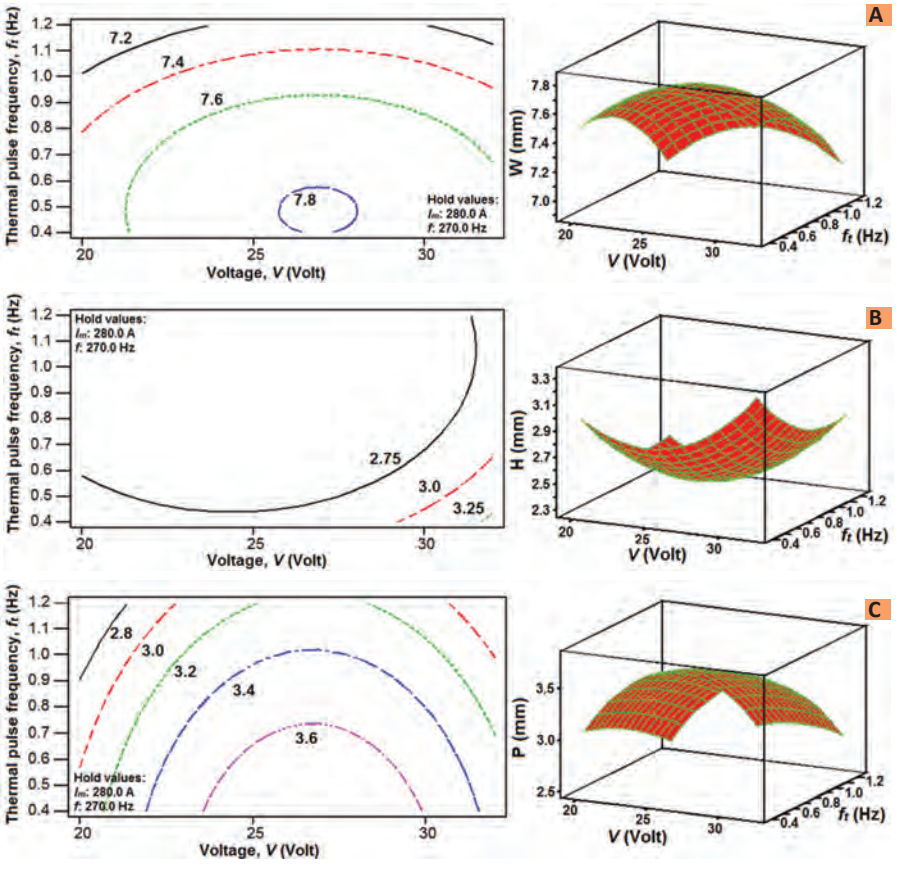

Fig. 16 — Contour and surface plot shows the effect of f_t and V on the following: A —bead width; B — bead height; C — depth of penetration: at constant values of I_m = 280 A and f = 270 Hz.

with temperature across the free surface of the weld pool, ($\delta\gamma/\delta T$) have contributed significant effect on the control of weld pool dimension and shape (Refs. 34, 36–42). In this context, Heiple and Roper (Refs. 43, 44) have mentioned that $\delta\gamma/\delta T$ is negative for most of the metals and the Marangoni force drives fluid flow on the surface outwards; however, the presence of surface active elements will produce a positive $\delta\gamma/\delta T$ which causes flow of the surface toward the center of the pool and subsequent increase in weld penetration. Matsunawa (Ref. 45) has also shown that for long arcs and welding currents higher than 200 A, viscous drag from the arc plasma can induce fluid flow in the weld pool. However, the detail derivations of these forces are beyond the scope of the present study and mentioned elsewhere by Zacharia et al. (Ref. 34).

In the present study, increasing mean current at high *f* (more than 200 Hz) (Fig. 11) has caused an increase in Lorentz force within the weld pool. Such high Lorentz force developed in the weld pool increases the downward motion, also known as forced vortex motion (Ref. 35), of the molten fluid and transmits heat directly to the bottom of the weld pool leading to deeper primary penetration. Nevertheless, several researchers (Refs. 46, 47) have demonstrated that due to the turbulent nature of the fluid flow in weld pool, as schematically shown in Fig. 18A, Lorentz force alone is unable to describe the nature of total fluid flow mechanism.

Therefore, it is certain that the Marangoni force and Lorentz force acted together on the flow field to control the effective weld pool area. Because of the increasing I_m, the surface temperature of the weld pool increases, and Kou and Wang (Ref. 48) have already reported that the increase in temperature decreases the surface tension, which ultimately leads to more negative surface tension temperature gradient ($\delta\gamma/\delta T$). More negative $\delta\gamma/\delta T$ pushes the molten fluid at the outward direction (away from the weld

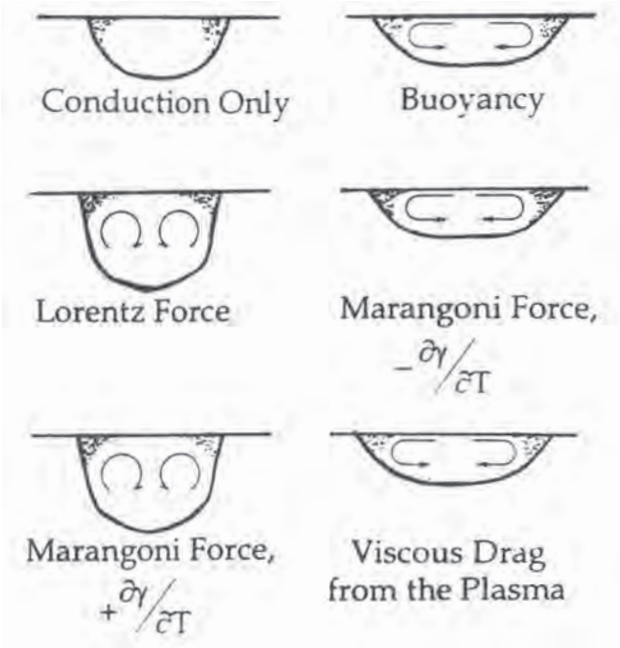

Fig. 17 — Schematic diagrams of the flow induced in the weld pool by individual driving forces and their effect on the weld pool shape.

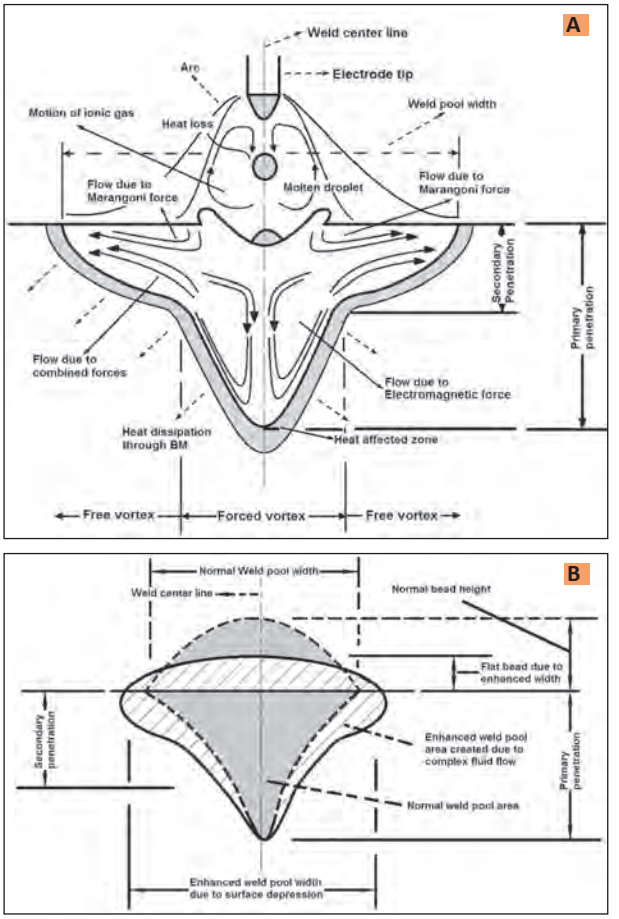

Fig. 18 — Schematic representations show the following; A — the effect of turbulent fluid flow induced in the weld pool by the combined result of different driving forces on the weld pool dimension and shape; B — the difference between conventional or normal bead geometry (i.e. not significantly affected by the complex fluid flow and generally occurs at the lower I_m and f level) and flat bead geometry (created due to surface depression at higher I_m and f level).

pool center as shown in Fig. 18A). The fluid motion in the outward direction is also referred to as free vortex motion after Lin and Eager (Ref. 35). Consequently, the forced and free vortex together can result in a complex flow pattern in the weld pool resulting in enhanced penetration profile with higher weld pool width (Fig. 8) because of deep surface depression (Ref. 35). In contrast, the weld pool width initially decreases (Fig. 13) with an increase of pulse frequency due to shortening of the pulsing time at the lower mean current (less than 250 A), which reduces the effective arc heat (Ref. 49).

However, at higher mean current (more than 270 A) due to higher energy density of the heat source weld pool width increases (Ref. 50). The increasing pulse frequency at high I_m (more than 270 A) reduces the peak duration between the pulses and thus reduces the droplet radius or size. The increase in *f* also increases the rate of droplet detachment due to higher number of droplets at fixed time duration. Small droplet radius with high I_m simultaneously reduces the surface tension force and induces the outward or free vortex fluid flow, which increases the weld pool width. Again, one should also consider the effect of thermal pulse frequency along with *f* on the fluid flow. Lower f_t at high I_m (more than 270 A) and *f* (more than 200 Hz) (Figs. 11 and 13) increases the thermal peak duration and increases the number of high-frequency pulses or drop transfer rate, which probably increases the free vortex fluid flow, and thus enhances bead width. Again, high-thermal peak duration also increases the arc temperature and the mobility of ions present in the arc, which results in higher arc force. Higher ionic mobility or the arc force increases the impact force of droplet due to higher droplet velocity and/or acceleration. Liu et al. (Refs. 11, 12) recently showed that the higher impact force of thermally exited molten drops can create more pinch effect on the weld puddle and transmit maximum heat at the bottom, which could cause higher primary penetration. These combined effects of the driving forces, as a result of different I_m, *f*, and f_t , increases the weld pool area (consists of weld pool width, secondary and primary penetration all together), which causes higher bead width and depth of penetration.

On the other hand, decreasing weld reinforcement or bead height is closely dependent upon the resultant interaction between Lorentz force and Marangoni force. In fact, high forced and free vortex motion have created increased surface curvature or the weld cavity as shown in Fig. 18B, which eventually resulted in deep surface depression. Since at a given process parameter the volume of the molten metal remains unchanged, the molten metal from top surface took part in filling up the excess weld cavity created by high forced and free vortex. This phenomenon incurred shallower reinforcement (Fig. 18B), and hence, decreased the bead height (Ref. 31). Interestingly, in the present study, with decrease in reinforcement or bead height of the weld deposits, both bead width and depth of penetration increased.

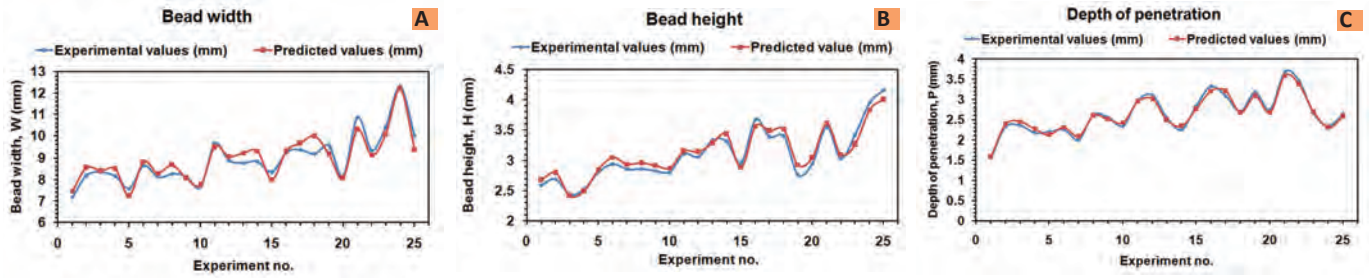

Fig. 19 — Comparison of weld bead geometry. A — Width; B — Height; C — Depth of penetration, between experimental values and predicted (using RSM model) values.

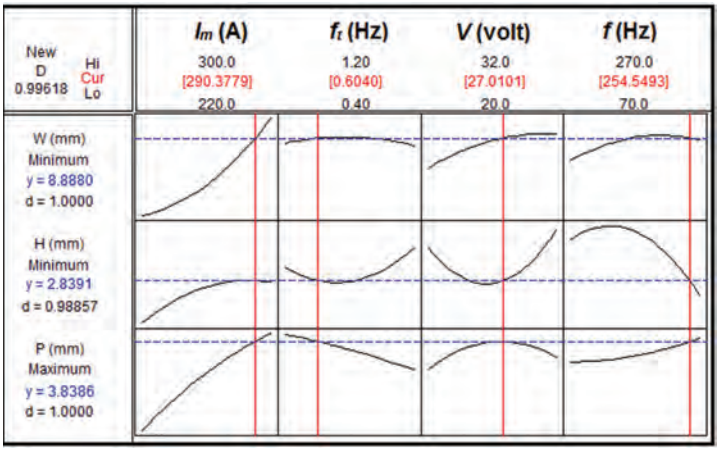

Fig. 20 — Optimization plot for combined optimization of bead geometry.

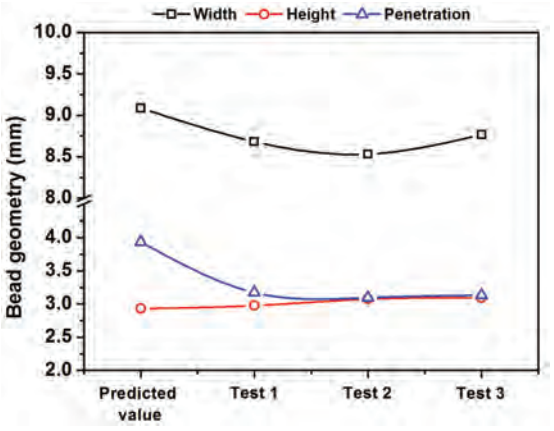

Fig. 21 — Verification results for the bead geometry comparing response surface model with experiments.

Second-Order Polynomial Model for Bead Geometry

The second-order polynomial multiple regression model shows that the different bead geometry (Y, mm) can be expressed as the function of DP-GMAW process parameters such as I_m, f, f_t, and V. The relationship between the bead geometry and the process parameters is expressed as follows:

$$Y = \beta_0 + \beta_1 \times I_m + \beta_2 \times f + \beta_3 \times f_t + \beta_4 \times V + \beta_{11} \times I_m^2 + \beta_{22} \times f^2 + \beta_{33} \times f_t^2 + \beta_{44} \times V^2 + \beta_{12} \times I_m \times f + \beta_{13} \times I_m \times f_t + \beta_{14} \times I_m \times V + \beta_{23} \times f \times f_t + \beta_{24} \times f \times V + \beta_{34} \times f_t \times V \quad (8)$$

From the observed data for the bead geometry and DP-GMAW process parameters (Tables 3 and 4) using Equation 8, the second-order response functions are determined below.

$$\text{Width (W, mm)} = 18.983 - 0.135 \times I_m + 0.014 \times f - 0.944 \times f_t + 0.180 \times V + 0.0002 \times I_m^2 - 0.00000246 \times f^2 - 1.054 \times f_t^2 - 0.0007 \times V^2 - 0.00005 \times I_m \times f + 0.009 \times I_m \times f_t + 0.001 \times I_m \times V - 0.00063 \times f \times f_t + 0.0000025 \times f \times V - 0.000013 \times f_t \times V \quad (9)$$

$S = 0.4075$ $R^2 = 95.2\%$ R^2 (adjusted) $= 79.8\%$

$$\text{Height (H, mm)} = -0.147 + 0.052 \times I_m + 0.021 \times f - 5.084 \times f_t - 0.369 \times V - 0.00006 \times I_m^2 - 0.00002 \times f^2 + 1.068 \times f_t^2 + 0.009 \times V^2 - 0.00003 \times I_m \times f + 0.0011 \times I_m \times f_t - 0.00048 \times I_m \times V + 0.001 \times f \times f_t + 0.000099 \times f \times V + 0.00068 \times f_t \times V \quad (10)$$

$S = 0.1543$ $R^2 = 95.9\%$ R^2 (adjusted) $= 81.8\%$

$$\text{Penetration (P, mm)} = -21.54 + 0.09 \times I_m - 0.04 \times f + 11.08 \times f_t + 0.73 \times V - 0.00006 \times I_m^2 + 0.00001 \times f^2 - 0.41 \times f_t^2 - 0.02 \times V^2 + 0.00003 \times I_m \times f - 0.04 \times I_m \times f_t + 0.0008 \times I_m \times V + 0.00209 \times f \times f_t + 0.0000679 \times f \times V - 0.0000585 \times f_t \times V \quad (11)$$

$S = 0.3356$ $R^2 = 96.1\%$ R^2 (adjusted) $= 86.0\%$

A result of ANOVA for the response surface function of the bead geometry is shown in Tables 5–7. By comparing with the calculated and the statistical F-ratios, it was seen that the second-order response function was quite adequate. Also the P-values of these models clearly point out the acceptability of the second-order regression equations. All the adjusted R^2 values are more than 79%, which is again a clear indication of the adequacy of the developed models. The values of weld bead geometry obtained from experiments and those predicted from response surface model are plotted in Fig. 19A–C. From the graph, it can be observed that the weld bead geometry obtained from experiments and those predicted by RSM are very close except for a few combination of parameters.

Optimization of Process Parameters

Optimization procedure in RSM is initiated by picking several starting points, from which, searching for the optimal factor is continued. Two types of solutions are obtained for the

search: 1) local solution, for each starting point there is a local solution. These solutions are the "best" combination of factor settings found for that particular starting point. 2) Global solution, there is only one global solution, which is the best of all the local solutions. The global solution is the "best" combination of factor settings for achieving the desired responses.

As for welding, the desirable weld bead geometry is one that has maximum depth of penetration, minimum or targeted bead width and bead height. The same can be achieved by adopting a multiobjective optimization procedure with global solution. To identify the combination of input variable settings that collectively optimize the above set of responses (i.e., W, H, and P), a response optimizer based upon the fitted model in RSM was utilized. The optimization was carried out using *Minitab*®, with multiple objectives viz., maximizing the depth of penetration, minimizing bead width, and minimizing bead height. The second-order polynomial models (Equations 9–11) are used to optimize responses with the set weight factor variable of "1" for each response. The optimum parameter settings so obtained for achieving the above objectives are: I_m = 290.37 A, f = 254.55 Hz, f_t = 0.6 Hz, and V = 27 V, and the corresponding optimization plot is depicted in Fig. 20. It is worthwhile to mention here that the obtained optimum process parameters using RSM optimization process were further checked for adequacy by comparing predicted value of bead geometry and experimental trials.

Confirmation Experiments

In confirmation of the second-order polynomial model (Equations 8–10), three verification tests (designated as Test 1, Test 2, and Test 3) were conducted using the optimum process parameters, which were determined by the response surface method to evaluate the optimal bead geometry. As shown in Fig. 21, differences between the predicted bead geometry (i.e., bead width, bead height, and depth of penetration), by the second-order response surface and the measure result by the experiments are small. Therefore, it can be concluded that the second-order response model is very useful for predicting the bead geometry. However, fluctuation occurred due to the redundant parametric variation during the welding operation. These fluctuations can be neglected if they remain within the tolerable limit (i.e., ± 5% of the respective predicted values).

Conclusions

The major conclusions are summarized below.

1) Bead width, bead height, and depth of penetration increases with increase in mean current (I_m) at fixed thermal pulse frequency (f_t). At a higher I_m level (above 250 A), bead width (W) is less sensitive to change in f_t , whereas bead height (H) increases with increase in f_t and large depth of penetration (P) can be achieved at lower $f_t$values. However, this variation was found to be reversed with a decrease in mean current at a constant thermal pulse frequency, especially for bead height and depth of penetration.

2) At a higher mean current level the increase in arc voltage (V) increases bead width of the weld deposit up to a certain level. Bead height initially decreases with an increased arc voltage at particular mean current level and then increases. It is also observed that at a particular mean current, the depth of penetration increases with an increase up to 25–28 V and then decreases with a further increase in arc voltage.

3) The pulse frequency (f) has twofold effects on bead geometry. Lower pulse frequency (ranging from 70 to 170 Hz) at higher mean current significantly increases W and H, but the effect of pulse frequency on W and H become opposite as the frequency increases further. On the other hand, depth of penetration at lower pulse frequency can be high if the I_m is also high, but at higher I_m increases in f significantly increases the penetration. It is also observed that maximum depth of penetration along with the lower bead width and height can be obtained within a particular range of pulse frequency and thermal pulse frequency (i.e., f = 200–260 Hz; f_t = 0.4–0.8 Hz).

4) From the whole study, it can be concluded that at a particular range of arc voltage (i.e., 25–28 V) higher mean current, higher pulse frequency along with lower thermal pulse frequency are able to produce optimum conditions for high depth of penetration with low or moderate bead width and height.

5) A second-order mathematical model was developed to predict the weld bead geometry. The acquired mathematical model has been checked by ANOVA for its adequacy. It was also found that the predicted bead geometry values using the mathematical model are compatible with the 25 experimental weld runs, which eventually signifies the success of the second-order mathematical model.

6) Response surface methodology is also used for optimization of process parameters. The optimum parameter settings so obtained for range of parameters used in this study are: I_m = 290.37 A, f = 254.55 Hz, f_t = 0.6 Hz, and V = 27. The optimum process parameters achieved from RSM was compared with experimental results. It was found that the predicted optimum bead geometry correlate very well with the confirmation test results.

7) Finally, it can be generalized that the obtained second-order polynomial models may be useful to predict bead geometry for any other double pulse arc welding processes within a range of input parameters, i.e., I_m = 220–300 A, f = 70-270 Hz, f_t = 0.4-1.2 Hz, and V = 20–32 V.

Acknowledgments

The authors express their sincere thanks to KEMPPI, Finland for donating the DP-GMAW power source and infrastructure to carry out this work.

References

1. Harvey, R. C. 1995. Gas metal arc welding fume generation using pulsed current. *Welding Journal* 74(2): 59-s to 68-s.

2. Palani, P. K., and Murugan, N. 2006. Review — selection of parameters of pulsed current gas metal arc welding. *J. Mater. Process Technology* 172: 1–10.

3. Smati, Z. 1986. Automatic pulsed MIG welding. *Mater. Construct.* 18: 38r– 44r.

4. Giridharan, P. K., and Murugan, N. 2009. Optimization of pulsed GTA welding process parameters for the welding of AISI 304L stainless steel sheets. *Int. J. Adv. Manuf. Technology* 40: 478–489.

5. Pal, K., and Pal, S. K. 2011. Effect of

pulse parameters on weld quality in pulsed gas metal arc welding: A review. *Journal of Materials Engineering and Performance* 20: 918–931.

6. Pires, I., Quintino, L., and Miranda, R. M. 2007. Analysis of the influence of shielding gas mixtures on the gas metal arc welding metal transfer modes and fume formation rate. *Mater. Des.* 28: 1623–1631.

7. Zhang, Y. M., Liguo, E., and Kovacevic, R. 1998. Active metal transfer control by monitoring excited droplet oscillation. *Welding Journal* 77(9): 388-s to 395-s.

8. Xiao, J., Zhang, G. J., Chen, S. J., Wu, L., and Zhang, Y. M. 2013. Active droplet oscillation excited by optimized waveform. *Welding Journal* 92(7): 205-s to 217-s.

9. Xiao, J., Zhang, G. J., Zhang, W. J., and Zhang, Y. M. 2014. Active metal transfer control by utilizing enhanced droplet oscillation part 1: Experimental study. *Welding Journal* 93(8): 282-s to 291-s.

10. Xiao, J., Zhang, G. J., Zhang, W. J., and Zhang, Y. M. 2014. Active metal transfer control by utilizing enhanced droplet oscillation part II: Modeling and analysis. *Welding Journal* 93(9): 321-s to 330-s.

11. Liu, A., Tang, X., and Lu, F. 2013. Study on welding process and prosperities of AA5754 Al-alloy welded by double pulsed gas metal arc welding. *Mater. Des.* 50: 149–155.

12. Liu, A., Tang, X., and Lu, F. 2013. Weld pool profile characteristics of Al alloy in double-pulsed GMAW. *Int. J. Adv. Manuf. Technology* 68: 2015–2023.

13. Mendes da Silva, C. L., and Scotti, A. 2006. The influence of double pulse on porosity formation in aluminum GMAW. *J. Mater. Process. Technology* 171: 366–372.

14. Goyal, V. K., Ghosh, P. K., and Saini, J. S. 2009. Analytical studies on thermal behaviour and geometry of weld pool in pulsed current gas metal arc welding. *J. Mater. Process. Technology* 209: 1318–1336.

15. Benyounis, K. Y., and Olabi, A. G. 2008. Optimization of different welding processes using statistical and numerical approaches — A reference guide. *Advances in Engineering Software* 39: 483–496.

16. Zhang, W., Liu, Y., Wang, X., and Zhang, Y. M. 2012. Characterization of three-dimensional weld pool surface in GTAW. *Welding Journal* 91(7): 195-s to 203-s.

17. Liu, Y. K., Zhang, W. J., and Zhang, Y. M. 2013. Estimation of weld joint penetration under varying GTA pools. *Welding Journal* 92(11): 313-s to 321-s.

18. Liu, Y. K., and Zhang, Y. M. 2013. Control of 3D weld pool surface. *Control Engineering Practice* 21: 1469–1480.

19. Pal, S., Malviya, S. K., Pal, S. K., and Samantaray, A. K. 2009. Optimization of quality characteristics parameters in a pulsed metal inert gas welding process using grey-based Taguchi method. *Int. J. Adv. Manuf. Technology* 44: 1250–1260.

20. Roy, R. K. 2001. *Design of Experiments Using the Taguchi Approach*. Wiley: New York.

21. Tarng, Y. S., Juang, S. C., and Chang, C.H. 2002. The use of grey-based Taguchi methods to determine submerged arc welding process parameters in hardfacing. *J. Mater. Process Technology* 128: 1–6.

22. Pan, L. K., Wang, C. C., Wei, S. L., and Sher, H. F. 2007. Optimizing multiple quality characteristics via Taguchi method-based Grey analysis. *J. Mater. Process Technology* 182: 107–116.

23. Sathiya, P., Abdul Jaleel, M. Y., Katherasan, D., and Shanmugarajan, B. 2011. Optimization of laser butt welding parameters with multiple performance characteristics. *Opt. Laser Technology* 43: 660–673.

24. Montogomory, D. C. 2001. *Design and Analysis of Experiments*. 5th edition, Wiley: New York.

25. Correia, D. S., Gonçalves, C. V., da Cunha, Jr., S. S., and Ferraresi, V. A. 2005. Comparison between genetic algorithms and response surface methodology in GMAW welding optimization. *J. Mater. Process Technology* 160: 70–76.

26. Khuri, A. I., and Cornell, J. A. 1996. *Response Surfaces; Design and Analysis*. Marcel Dekker: New York.

27. Anawa, E.M., and Olabi, A.G. 2008. Optimization of tensile strength of ferritic/austenitic laser-welded components. *Opt. Lasers Eng.* 46: 571–577.

28. Murugan, N., and Parmar, R. S. 1997. Effect of welding conditions on microstructure and properties of type 316L stainless steel submerged arc welding cladding. *Welding Journal* 76(5): 210-s to 220-s.

29. Gunaraj, V., and Murugan, N. 1999. Application of response surface methodology for predicting weld bead quality in submerged arc welding of pipes. *J. Mater. Process Technology* 88: 266–275.

30. Koleva, E. 2005. Electron beam weld parameters and thermal efficiency improvement. *Vacuum J.* 77: 413–421.

31. Goyal, V. K., Ghosh, P. K., and Saini, J. S. 2009. Analytical studies on thermal behaviour and geometry of weld pool in pulsed current gas metal arc welding. *J. Mater. Process Technology* 209: 1318–1336.

32. Allen, D. J., and Degnan, G. 1994. An investigation of fusion quality in conventional MIG, synergic pulsed MIG, flux cored arc and manual metal arc welding. *Conf. Proc. of EUROJOIN 2*, 191–202.

33. Essers, W. G., and Walter, R. 1981. Heat transfer and penetration mechanisms with GMA and plasma-GMA welding. *Welding Journal* 60(2): 37-s to 42-s.

34. Zacharia, T., Eraslan, A. H., Aidun, D. K., and David, S. A. 1989. Three-dimensional transient model for arc welding process. *Metall. Trans. B* 20B: 645–659.

35. Lin, M., and Eager, T. W. 1985. Influence of arc pressure on weld pool geometry. *Welding Journal* 64(6): 163-s to 169-s.

36. Zacharia, T., Eraslan, A. H., and Aidun, D. K. 1988. Modeling of non-autogenous welding. *Welding Journal* 67(1): 18-s to 27-s.

37. Zacharia, T., David, S. A., and Vitek, J. M. 1991. Effect of evaporation and temperature dependent material properties on weld pool development. *Metall. Trans. B* 22B: 233–241.

38. Oreper, G. M., Eager, T. W., and Szekely, J. 1983. Convection in arc weld pool. *Welding Journal* 62(11): 307-s to 312-s.

39. Kou, S., and Sun, D. K. 1985. Fluid flow and weld penetration in stationary arc welds. *Metall. Trans. A* 16A: 203–213.

40. Tsai, M. C., and Kou, S. 1989. Marangoni convection in weld pools with a free surface. *Int. J. Numer. Meth. Fluids* 9: 1503–1506.

41. Tsai, M. C., and Kou, S. 1990. Weld pool convection and expansion due to density variations. *Numer. Heat. Trans.* Pt A 17: 73–89.

42. Choo, R. T. C., Szekely, J., and David, S. A. 1992. On the calculation of the free surface temperature of gas-tungsten-arc weld pools from first principles: part II. Modeling the weld pool and comparison with experiments. *Metall. Trans. B* 23B: 371–384.

43. Heiple, C. R., and Roper, J. R. 1981. Effect of selenium on GTAW fusion zone geometry. *Welding Journal* 60(8): 143-s to 145-s.

44. Heiple, C. R., and Roper, J. R. 1982. Mechanism for minor element effect on GTA fusion zone geometry. *Welding Journal* 61(4): 97s to 102s.

45. Matsunawa, A. 1992. *Trends in Welding Research*, S. A. David, J. M. Vitek, eds., ASM International, Materials Park, Ohio, 3–16.

46. Malinowski-Brodnickka, M., and Ouden, G. D. 1990. Effect of electromagnetic stirring on GTA welds in austenitic stainless steel. *Welding Journal* 69(2): 52-s to 59-s.

47. Choo, R.T.C., and Szekely, J. 1994. The possible role of turbulence in GTA weld pool behavior. *Welding Journal* 73(1): 25-s to 31-s.

48. Kou, S., and Wang, Y. H. 1986. Weld pool convection and its effect. *Welding Journal* 65(3): 63-s to 70-s.

49. Ishida, T. 1992. Stainless steel modification on mild steel by pulsed current arc. *J. Mater. Sci. Lett.* 11: 83–85.

50. Tseng, K. H., and Chou, C. P. 2002. The effect of pulsed GTA welding on the residual stress of a stainless steel weldment. *J. Mater. Process Technology* 123: 346–353.